

Continuum Shielding and Flow Dynamics in Active Galactic Nuclei

Doron Chelouche^{*} and Hagai Netzer^{*}

*School of Physics and Astronomy and the Wise Observatory, The Beverly and Raymond Sackler Faculty of Exact Sciences,
Tel Aviv University, Tel Aviv 69978, Israel*

4 November 2018

ABSTRACT

We study the ionization, thermal structure, and dynamics of AGN flows which are partially shielded from the central continuum. We utilize detailed non-LTE photoionization and radiative transfer code using exact (non-Sobolev) calculations. We find that shielding has a pronounced effect on the ionization, thermal structure, and the dynamics of such flows. Moderate shielding is especially efficient in accelerating flows to high velocities since it suppresses the ionization level of the gas. The ionization structure of shielded gas tends to be distributed uniformly over a wide range of ionization levels. In such gas, radiation pressure due to trapped line photons can dominate over the thermal gas pressure and have a significant effect on the thermal stability of the flow. Heavily shielded flows are driven mainly by line radiation pressure, and so line locking has a large effect on the flow dynamics. We show that the observed “ L_α ghost” is a natural outcome in highly ionized flows that are shielded beyond the Lyman limit. We suggest that high velocity AGN flows occupy only a small fraction of the volume and that their density depends only weakly on the velocity field.

Key words: ISM: jets and outflows — galaxies: active — galaxies: nuclei — quasars: absorption lines — X-rays: general

1 INTRODUCTION

Gas outflows are common in astrophysical systems in general, and in active galactic nuclei (AGN) in particular. AGN flows span a wide range of ionization levels with spectral signatures extending from the optical to the X-ray band. Direct evidence for outflowing gas in type-I AGN comes from the detection of blueshifted absorption lines, with velocities ranging from a few $\times 100$ km s⁻¹ (so called narrow absorption line, NAL, flows) to more than 10,000 km s⁻¹ (broad absorption line, BAL, flows). X-ray observations show that AGN showing BAL-like features also have relatively weak soft X-ray flux (“soft X-ray weak QSOs”, SXWQ; Brandt, Laor, & Wills 2000). Among SXWQ, BALQSOs are extremely X-ray weak objects. Recent *Chandra* and *XMM* observations indicate that soft X-ray weakness results from intrinsic line-of-sight absorption by intervening material (e.g., Gallagher et al. 2002). The properties of the absorbing material are poorly constrained by current X-ray observations with only a few reliable measurements of the column density ($\gtrsim 10^{22}$ cm⁻²; e.g., Green et al. 2001). Similar uncertainties apply also to other flows (e.g., de Kool et al. 2001, Everett, Koenigl, & Arav 2002; see also Arav et al. 1999). UV NAL outflows and soft X-ray absorption by ionized gas are seen in many low luminosity type-I AGN (George et al. 1998, Crenshaw et al. 1999) and a possible physical connection between the two has been suggested by Mathur et al. (1994).

Like stellar winds, AGN outflows are thought to be driven by radiation pressure force (e.g., Arav, Li, & Begelman 1994, Koenigl & Kartje 1994, Murray, Grossman, Chiang, & Voit 1995, Proga, Stone, & Kallman 2001, and Chelouche & Netzer 2001; hereafter CN01, but see Begelman, de Kool, & Sikora 1991 for a different model). However, the differences in the geometry, the distance scales, and the underlying continuum between the groups are very large. A long standing issue concerns the fact that BAL flows have a relatively uniform ionization structure over a wide range of velocities. This can be explained theoretically if the flow is kept from becoming too dilute by means of a confining medium (e.g., Arav, Li, & Begelman 1994; but see Krolik 1979 and Mathews & Blumenthal 1977) or by means of continuum shielding (Murray et al. 1995, Proga et al. 2000). The latter is the focus of this paper.

This work is part of a series of papers investigating the ionization and dynamics of radiation pressure driven flows in AGN. In the first paper (Chelouche & Netzer 2003; hereafter CN03) we have developed a general non-Sobolev scheme for calculating the ionization and dynamics of AGN flows. Here we focus on the physics of shielded flows, i.e., those flows which are illuminated by a modified (absorbed) type-I AGN continuum. Specifically, we attempt to answer the following key questions: 1) What are the dominant ionization levels in shielded flows? 2) What governs the dynamics of shielded flows? 3) What is the preferred geometry of high velocity flows? 4) Can self-consistent photoionization and dynamical calculations account for the observed properties of BAL flows?

This paper is organized as follows: In section 2 we present the

* email: doron@wise.tau.ac.il; netzer@wise.tau.ac.il

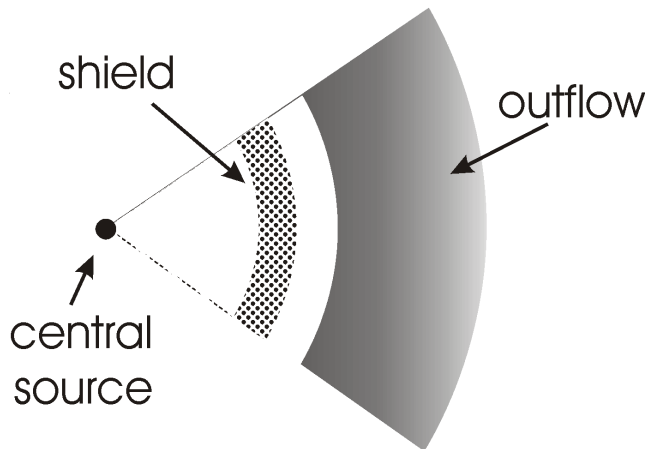


Figure 1. The flow–shield geometry. The shield is situated between the continuum source and the flow and may or may not be coupled, mechanically, to the flow. The ionizing flux impinging upon the flow is due to the transmitted continuum. It depends on U_x^{shield} and N_H^{shield} (see text). Spherical geometry is assumed.

general method and the basic assumptions. Results pertaining to the ionization level, thermal structure, and radiation pressure are given in section 3. The radiation pressure force is discussed in section 4. In section 5 we calculate the structure and dynamics of shielded flows, focusing on their velocity profiles and spectral features. The conclusions and summary are presented in section 6.

2 METHOD

Our aim is to study the effect of shielding on the dynamics, ionization, and thermal structure of radiation pressure driven photoionized flows in AGN. The motivation stems from observations as well as from previous theoretical studies which suggest the possible effect of shielding on the gas dynamics. Throughout this work we assume flows that are exposed to a modified type-I AGN ionizing continuum whose properties depend on shielding material (hereafter “the shield”) which lies between the ionizing source and the base of the flow. The shield–flow geometry is depicted in figure 1.

2.1 Self-consistent calculation of the flow structure and dynamics

This work focuses on the properties of radiation pressure driven flows as described in CN03. Below is a brief outline of the formalism and the reader is referred to CN03 for a more detailed description.

The equation of motion is

$$v \frac{dv}{dr} = \frac{1}{\rho} \left(F_{\text{rad}} - \frac{dP_{\text{tot}}}{dr} \right) - g(r), \quad (1)$$

where v is the velocity, r the radial coordinate, ρ the gas density, F_{rad} the radiation pressure force, P_{tot} the total pressure (the sum of gas and internal radiation pressure), and g the gravity. Both F_{rad} and P_{tot} depend on the ionization and thermal structure of the flow, which in turn depends on the ionization parameter, U_x , (the ratio of the photon density in the range 0.1–10 keV and the hydrogen number density), and the spectral energy distribution (SED) of the ionizing flux. In all calculations we assume low density flows ($< 10^{12} \text{ cm}^{-3}$). Thus, collisional processes are negligible (CN01).

Unless otherwise stated, we assume the following continuity condition,

$$\rho \propto r^{-2} v^{-1}. \quad (2)$$

The local radiation pressure force is calculated using the force multiplier formalism,

$$F_{\text{rad}}(r) = H_c M(r), \quad (3)$$

where

$$H_c = \max(n_H, n_e) \frac{\sigma_T L_{\text{tot}}}{4\pi r^2 c}, \quad (4)$$

σ_T is the Thomson cross-section, n_H the hydrogen number density, n_e the free electron number density, and L_{tot} the bolometric luminosity of the source. Note that by choosing $\max(n_H, n_e)$, instead of n_e , we allow for the Compton radiation pressure force in both ionized and neutral gas.

The force multiplier, $M(r)$, includes the contribution of all scattering and absorption processes: bound-bound - M_{bb} , bound-free - M_{bf} , and Compton scattering. Another useful parameter that has been used extensively in older, Sobolev-type calculations is the local electron scattering optical depth,

$$t = \max(n_H, n_e) \sigma_T v_s \left(\frac{dv}{dr} \right)^{-1}, \quad (5)$$

where v_s is the sound speed. This parameter converges to the usual definition of t that includes n_e instead of n_H for ionized gas and is suitable for both highly ionized and neutral flows.

The total pressure is the sum of gas pressure, P_{gas} and internal radiation pressure, P_{rad} , due to scattering of resonance line photons (Elitzur & Ferland 1986). We calculate P_{rad} according to the scheme outlined in CN03 which is suitable for differentially expanding flows with a finite optical depth.

The above scheme is used to obtain a self-consistent solution for the flow structure and dynamics given a set of initial conditions, r_0 , $U_x(r_0)$, L_{tot} , the initial velocity, v_0 , and the mass of the central object. We iterate between the photoionization and thermal equations, the radiation pressure force calculations, the equation of motion, and the continuity condition, until the density profile converges to less than 1%. Using this method, the mass flow rate is determined by the initial conditions and not from critical point analysis (see CN03).

2.2 The modified ionizing continuum

An important input for the calculations is the assumed SED. X-ray observations of SXWQ cannot constrain the ionization level of the intervening absorber. Signatures of highly ionized absorbing gas are common in type-I objects and recent works (e.g., Proga, Stone, & Kallman 2001) show that this may also be the case in SXWQ. In this work we model the shield as a uniform slab whose properties are defined by its ionization parameter, U_x^{shield} and column density, N_H^{shield} . This allows us to study a wide range of shield properties. We assume that the shield completely covers the ionizing source and is static (i.e., absorption lines with thermal widths).

The shield is exposed to a typical type-I AGN continuum with a UV bump, $\alpha_x = 0.9$ and $\alpha_{ox} = 1.4$ ($L_E \propto E^{-\alpha}$, see CN01 and references therein). We calculate the self-consistent ionization and thermal structure of the shield using ION 2002, the 2002 version of the photoionization code ION (Netzer 1996), and obtain the transmitted spectrum through the shield, ignoring emission features.

Our thermal calculations include the effect of adiabatic cooling which depends on dv/dr and v/r . We find that, in general,

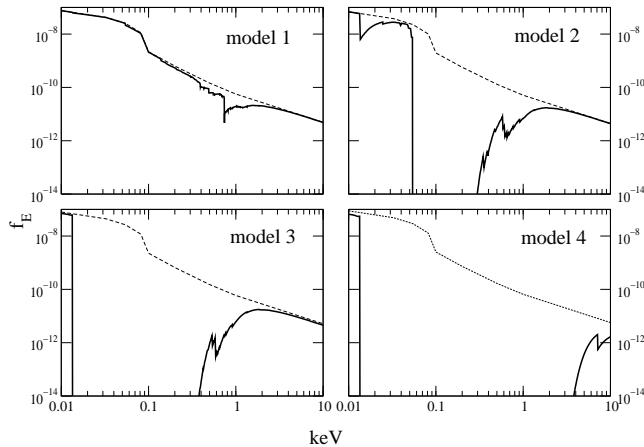


Figure 2. The four shielded continua used in this work. Note the heavy X-ray absorption of model 4 where the continuum recovers only beyond ~ 10 keV. Model 1 has typical warm absorption features (O VII and O VIII edges). The dashed line marks the intrinsic type-I SED used in this work.

No.	U_x^{shield}	N_H^{shield} (cm^{-2})	comments
1	10^{-1}	10^{22}	warm absorption
2	$10^{-2.5}$	10^{22}	optically thick He II edge
3	10^{-3}	10^{22}	optically thick H I & He II edges
4	10^{-3}	10^{24}	extreme neutral shielding

Table 1. Definition of the shielding models used in this work.

adiabatic cooling can be neglected for sub-relativistic flows close to the AGN ($r < 100$ pc). Flows which lie at larger distances are probably not in photoionization equilibrium and shall not be treated in this work.

We define four types of modified continua that are shown in figure 2 and are defined in table 1. Model 1 has prominent “warm absorption” features due to O VII and O VIII edges. Model 2 is optically thick beyond the He II edge, and recovers above ~ 1 keV. Models 3 and 4 are optically thick above the H I edge and recover at ~ 1 keV and ~ 10 keV, respectively. We have also explored a set of neutral shields that are commonly used in X-ray spectral modelling (e.g., the WABS model in XSPEC; e.g., George et al. 1998).

In our shielded flow models, P_{tot} and F_{rad} depend on U_x and the SED. In order to allow a meaningful comparison between flows that are exposed to different continua, we have changed the definition of U_x to denote *the value of the ionization parameter which would be defined for unshielded gas at the same location and with the same density*.

3 IONIZATION, TEMPERATURE AND PRESSURE OF SHIELDED OUTFLOWING GAS

3.1 General considerations for neutral shields

We first study the effect of neutral shielding assumed to be most relevant to SXWQ. Figure 3 shows the dependence of the ionization structure of H I, He II and O VIII for shielded gas with $U_x = 0.1$ on the properties of the neutral shield. As shown, the level of ionization of such gas drops with increasing N_H^{shield} . For $N_H^{\text{shield}} \sim 10^{22} \text{ cm}^{-2}$, the O VIII abundance drops by almost

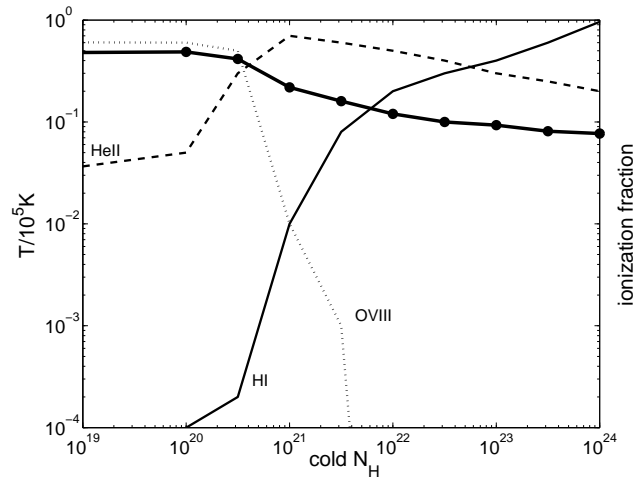


Figure 3. The temperature (in units of 10^5 K) and ionization structure of H I, He II, and O VIII in shielded gas with $U_x = 0.1$ as a function of N_H^{shield} for shielding by neutral material. Note the sharp drop in temperature and in O VIII fraction for $N_H^{\text{shield}} \gtrsim 10^{21} \text{ cm}^{-2}$. For $N_H^{\text{shield}} \gtrsim 10^{22} \text{ cm}^{-2}$, the gas is almost completely neutral.

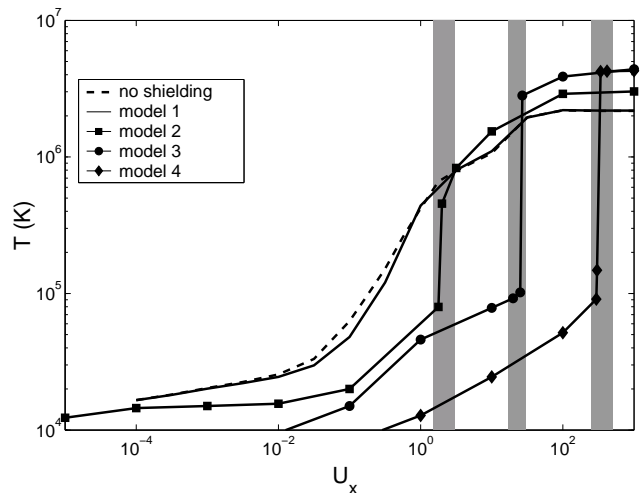


Figure 4. The temperature of photoionized gas as a function of U_x for various shielding models. As shielding increases, the temperature is reduced and higher temperatures require larger U_x . Note the sharp transition to high temperatures designated by the shaded areas. The dashed curve corresponds to unshielded gas.

two orders of magnitude and the ionization level resembles that of the broad line region (BLR). The temperature traces the ionization level of the flow and decreases by a factor ~ 4 from small column density shields to the $N_H^{\text{shield}} = 10^{22} \text{ cm}^{-2}$ shield.

3.2 Thermal structure and stability

The temperature of the shielded gas as a function of U_x is shown in figure 4 for all four models. Warm absorption-type shield (model 1) has only a small and localized effect on the ionization and the temperature of the shielded gas. When shielding increases (model 2), the reduction in electron temperature is more pronounced due to the large deficit in ionizing photons. However, above some critical U_x ($U_x > 1$ for model 2), the temperature climbs quickly to the

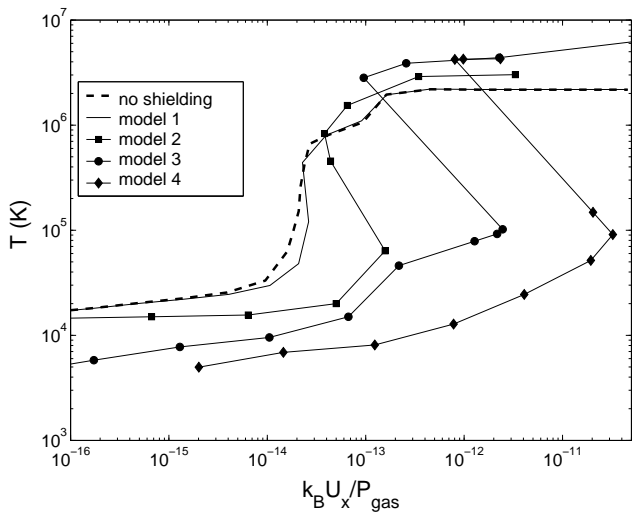


Figure 5. Thermal stability curves for various shielded flows. The instability regions (the sections with negative derivatives) occupy only a small range in U_x (the shaded areas in figure 4). The dashed curve corresponds to an unshielded case. (k_B is the Boltzmann constant).

Compton temperature which is slightly above the temperature of the unshielded gas due to the different mean photon energy. Shielding above the H I edge (model 3) suppresses the temperature up to $U_x \simeq 10$. In this case, the shielded gas is neutral up to $U_x = 10^{-2}$. For the largest shielding (model 4), the gas is almost neutral up to $U_x \sim 10^2$. Thus, heavily shielded gas that shows absorption features due to O VII and O VIII edges is $\sim 10^3$ (!) times more dilute than non-shielded gas at the same location showing the same features.

Figure 4 shows also the presence of a critical ionization parameter, $U_x^{\text{crit.}}$ (marked by shaded areas) for the shielded gas, beyond which the gas temperature climbs to the Compton temperature. Heavier shielding results in large $U_x^{\text{crit.}}$. The reason for the sharp rise in temperature over a narrow U_x range ($\Delta U_x / U_x^{\text{crit.}} \ll 1$) is the peculiar ionization structure of He II. When He II abundance is large, the temperature is low so recombination cooling is effective and the gas remains at low temperatures (see also Stevens 1991). Once $U_x^{\text{crit.}}$ is reached, He II ionizes, the temperature rises, recombination becomes less effective, most metals ionize and the cooling rate decreases sharply. Under these conditions, the gas reaches its Compton temperature.

While photoelectric absorption from excited levels is negligible for unshielded non-LTE gas, this is not the case for heavily shielded, partly ionized gas (e.g., models 3 and 4) with large U_x . Under these conditions, continuum pumping can populate the excited levels in regions of small optical depth.

Shielding and internal radiation pressure can have a profound effect on the thermal stability curve of photoionized, shielded gas. We first show the effect of shielding alone and then incorporate the effects of internal radiation pressure.

Shielding of photoionized gas enhances and extends its thermal instability (the part of the curve with $dT/d(U_x/P_{\text{gas}}) < 0$) due to the suppression of the UV flux. This is illustrated in figure 5. Given our intrinsic SED, non-shielded gas is thermally stable over the entire range of U_x . Model 1 shielding results in a small region of marginal stability (see also Marshall et al. 1993, Krolik & Kriss 2002). Increased shielding results in appearance of larger instability regions. These regions correspond to a narrow range in U_x

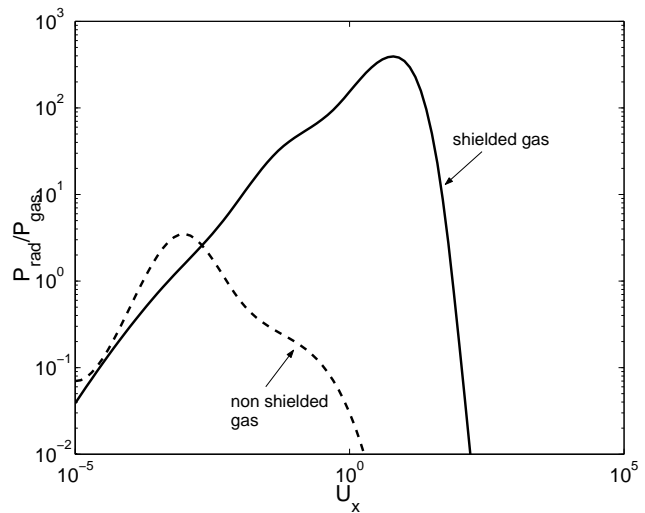


Figure 6. The ratio of radiation to gas pressure as a function of U_x for model 3 shielding and shielded gas which is optically thick to resonance lines (see text). For highly ionized shielded gas ($U_x \simeq 1$) radiation pressure dominates the total pressure. For low U_x , $P_{\text{gas}} \gg P_{\text{rad}}$ due to the low ratio of photon to gas density. When U_x is large, the gas is fully ionized and scattering of line photons is negligible. Note the large difference in the contribution of P_{rad} to the total pressure between shielded and non-shielded gas.

($\Delta U_x / U_x^{\text{crit.}} \ll 1$; the shaded areas in figure 4). The shape of the stability curves for heavily shielded flows is relatively independent on the shape of the intrinsic SED.

We considered in detail the effect of P_{rad} on the thermal stability of the gas. The exact value of P_{rad} depends on the global properties of the flow (temperature, ionization structure and dynamics), and on the shield–flow configuration. To simplify the problem and to obtain an upper limit on this effect, we focus on the extreme case where the base of the flow and the shield are co-moving with no differential motion. We assume that the flow has a uniform ionization structure and is optically thick to resonance line absorption (in particular L_{α} , C IV $\lambda 1549$, He II $\lambda 304$). This results in the largest possible P_{rad} (see figures 7, 8 in CN03). In figure 6 we show the contribution of P_{rad} to P_{tot} . P_{rad} is larger than P_{gas} by more than two orders of magnitude for highly ionized shielded gas with substantial line opacity. This result is very different from the typical values obtained for non-shielded gas (CN03) for the following reasons: For a given U_x , the level of ionization of a shielded gas is always lower than the ionization level of a non-shielded gas. This means more optically thick lines and, hence, larger P_{rad} . For very large U_x , even the shielded gas is ionized and P_{rad} drops accordingly.

Isobaric perturbations lie, by definition, along a $P_{\text{tot}} = \text{const.}$ curve (see Bottorff et al. 2001 for instructive discussion on stability curves). We therefore carried the same stability analysis substituting P_{tot} for P_{gas} in the abscissa of figure 5. The new stability curves for model 2 and 3 shielding are shown in figure 7. The inclusion of P_{rad} significantly alters the shape of the stability curve and narrows the range of ionization parameter where thermal instabilities occur. These newly calculated stability curves illustrate the maximum deviation from a $P_{\text{tot}} = P_{\text{gas}}$ stability curve since dynamical effects within the flow and between the flow and the shield have not been included. Specific flow models would therefore lie within the shaded area bounded by the two extreme stability curves (including and excluding the maximum P_{rad}). Figure 7 shows that

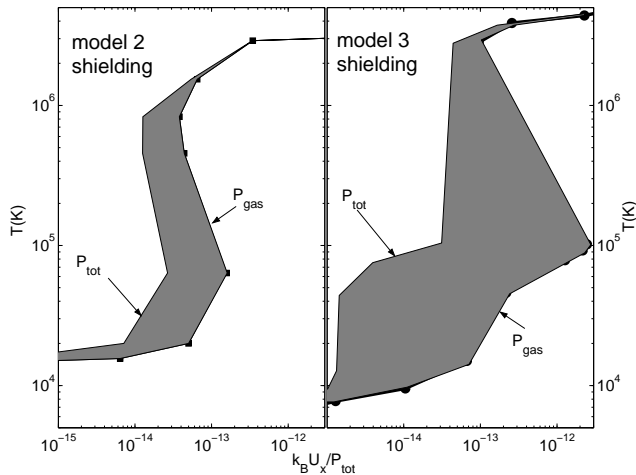


Figure 7. The effect of line pressure on the stability curve for model 2 (left panel) and model 3 (right panel) shielding. Both diagrams refer to a static configuration (see text). The stability curves of all flows whose opacity is small compared to the shield opacity lie within the shaded area. Some of those curves can be thermally stable for the entire range of U_x .

it is possible, in principal, to have a flow configuration which is thermally stable for all values of U_x . This stabilizing effect is especially important for low velocity, optically thick flows. We note that P_{rad} cannot suppress isobaric perturbation with wavelength λ_p ($\delta T \propto e^{i2\pi r/\lambda_p}$) shorter than the mean free path of the photon in the gas. This is the physical length corresponding to a line optical depth of ~ 1 .

3.3 The ionization structure

Next we study the effect of shielding on the ionization structure of the gas. We demonstrate this by showing the oxygen ionization structure. This is shown in figure 8. As expected, the deviations of the ionization structure from the unshielded case are more pronounced for heavier shielding. For example, O III is very abundant up to $U_x < 10^{-3}$ for unshielded gas, but remains abundant up to $U_x = 100$ for model 4 shielding.

Shielding has another important effect on the ionization structure of the gas. For non shielded gas, the ionization structure of oxygen is dominated by the three most abundant ions, each with an ionization fraction of ~ 0.3 . This is shown, for example, in figure 8a for $U_x = 0.01$ where most oxygen is O V, O VI, and O VII. As shielding increases, the distribution of ionization levels is wider (see the knee which develops in figures 8b-d as the contours become vertical at high U_x). A most extreme example is that of figure 8d where for $U_x \simeq 100$, the oxygen ionization structure is very uniform with O III–O VIII all having similar fractional ionizations of ~ 0.1 . The reason for this peculiar ionization structure is the shape of the modified SED which shields O II and higher ionization levels from the ionizing UV photons, but allows X-ray photons to penetrate the gas and cause inner shell ionization. The density of the X-ray photons above the K ionization edge is similar for all oxygen ions and the distribution among the various ions is more uniform. Thus, heavily shielded gas may show a myriad of ionization levels all coming from the same location. This may explain the wide range of ionization levels observed in BAL flows.

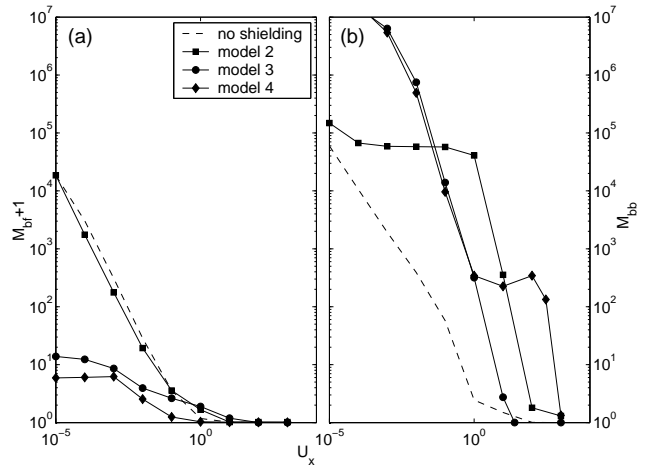


Figure 9. The effect of shielding on the radiation pressure force (a) due to continuum processes (M_{bf}) and (b) due to lines (M_{bb}). Note the decline of the radiation pressure force with U_x for all models. Note also the increase of M_{bb} and the decrease of M_{bf} with shielding (see text). The results for non-shielded cases are shown for comparison (dashed line).

4 THE RADIATION PRESSURE FORCE

Here we study the effect of shielding on the radiation pressure force. We focus on model 2–4 shielding since model 1 shielding has only a small effect. In the following diagrams the value of M is normalized to the Compton radiation pressure due to the non-shielded continuum in order to allow comparison between different shields.

Results for the bound-free (M_{bf}) and bound-bound (M_{bb}) force multiplier are shown in figure 9a and 9b. As shielding increases, M_{bf} decreases due to the growing deficit in UV photons that carry most of the momentum. This is more pronounced for low U_x and heavy shielding (model 3 and 4) where the largest contributions to M_{bf} are due to absorption by H I and He II. Contrary to M_{bf} , M_{bb} increases with shielding, especially for low U_x , since the main driving lines of low ionization species lie below the He II and H I edges, and are thus exposed to the unshielded continuum.

Next we study the effect of dynamics on the radiation pressure force. We do so by using the Sobolev t -parameterization (equation 5). This implicitly assumes the Sobolev approximation, i.e., ignoring line locking and line blanketing and discontinuities in the flow. As shown in figure 10, dynamics has a substantial effect on M_{bb} but a negligible effect on M_{bf} . M_{bb} declines with increasing t since many lines become optically thick and their contribution to M declines. This is most pronounced for models 3 and 4 and for low U_x where the largest contribution to M_{bb} are due to H I and He I absorption lines. Our calculations show that moderate shielding results in more efficient acceleration for large U_x and t due to the larger contribution of metal lines which become optically thick at a significantly larger t .

Table 2 lists the important lines that drive the flow for model 2 and 3 shielding and the case of $t = 10^{-4}$. We chose the value of U_x such that the temperature is similar in the two cases. This means an order of magnitude difference in U_x because of the very different shielding. For moderate shielding, the contribution of lines near the UV bump (around 250Å) is the largest. For heavy shielding, near UV and optical lines are the largest contributors to M_{bb} since the flux above the H I edge is negligible. X-ray lines also contribute to M_{bb} since the continuum recovers at around 2 keV. In all shielded

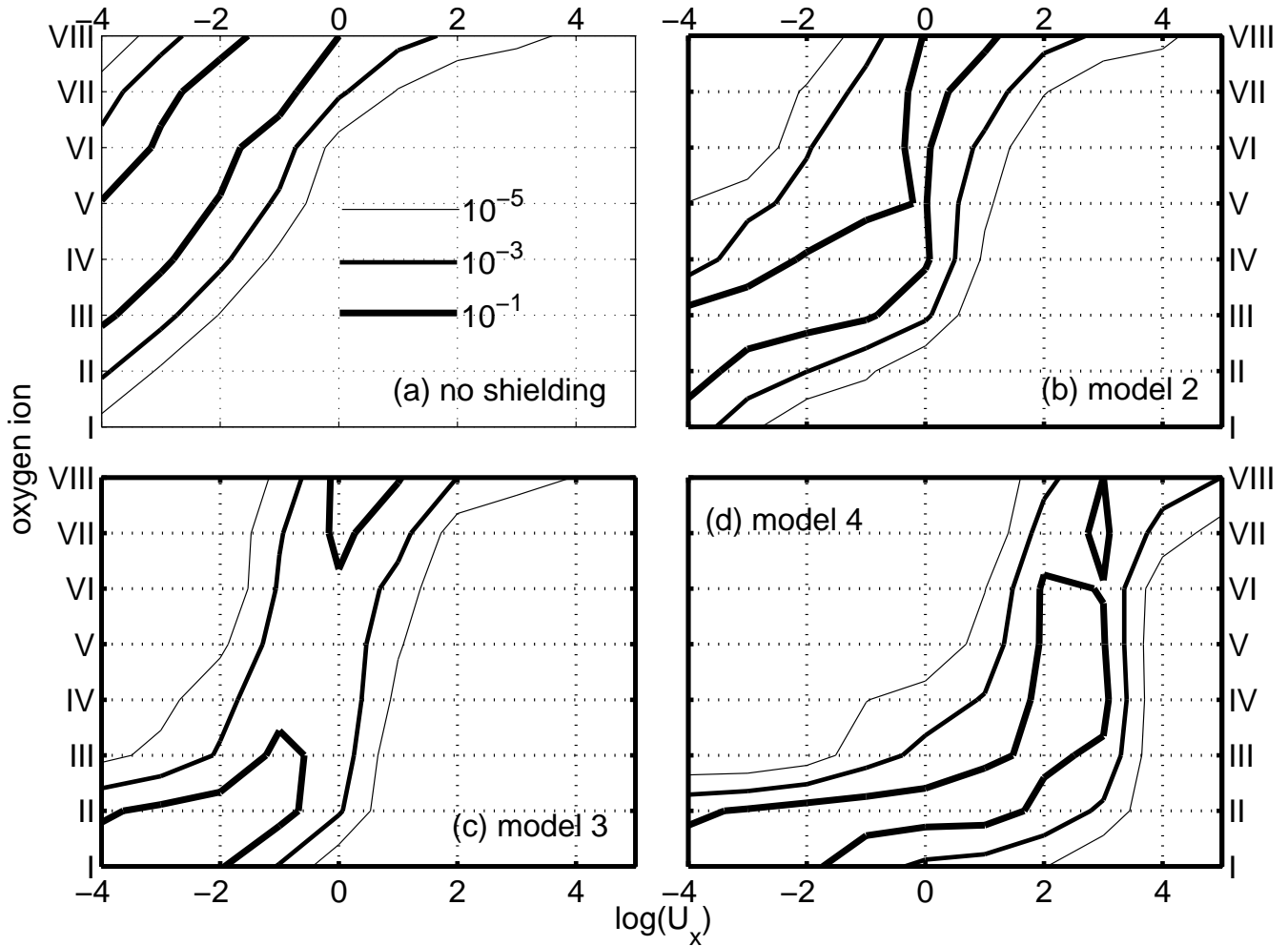


Figure 8. The fractional ionization of O I–O VIII as a function of U_x for gas which is exposed to (a) a non-shielded ionizing continuum, (b) model 2, (c) model 3, and (d) model 4 shielding. Each contour level (marked by a different line) represents two orders of magnitude in abundance (10^{-5} , 10^{-3} , 10^{-1}). As shielding increases, the neutral ionization structure extends to larger U_x and more oxygen ions have similar abundances at high ionization parameters (e.g., for model 4 shielding, all ions from O III to O VIII show the same abundances at $U_x \sim 100$).

flows, the main driving lines are very different from the driving lines in non-shielded cases and fewer lines contribute significantly to M_{bb} (see table 1 in CN03). The contribution of absorption from excited levels is negligible for such optically thick gas.

CN03 argued that the contribution of line locking to the total radiative acceleration is small in non-shielded AGN gas. Nevertheless, observations of C IV $\lambda 1549$ show that line locking in general, and that of L_α on N V $\lambda 1240$ in particular, can have a significant and observable effect on the dynamics of BAL flows (the so called “ L_α ghost phenomenon”; e.g., Korista et al. 1996, Arav et al. 1996). Arav (1996) argued that the effect of line locking can be important if optical and near UV lines are solely responsible for accelerating the gas. Below we discuss two issues related to line-locking: self-line locking where absorption lines are exposed to the peak of their corresponding emission lines, and L_α -N V $\lambda 1240$ line locking.

The effect of self locking for model 3 shielded flow is shown in figure 11. The diagram shows the ratio of M calculated with and without self locking as a function of U_x and t . The lines that are included are Mg II $\lambda 2799$, L_α , N V $\lambda 1240$, and O VI $\lambda 1035$ with properties as given in Telfer et al. (2002). We assume that emis-

sion and absorption line profiles have no relative shifts, i.e., maximum line locking. Comparing to the non-shielded case (figure 6 in CN03), we note that shielding increases the effect of line locking since, in this case, the number of lines that contribute significantly to M_{bb} is smaller. The contribution of $L_\alpha - L_\alpha$ locking is most pronounced for low ionization, optically thin gas, and can increase M by a large factor. This contribution is significantly smaller for larger U_x because of the drop in the H I abundance, and for large t ($t > 10^{-10}$) when L_α becomes optically thick. A most peculiar feature is a ridge with an almost constant ratio of ~ 2 , extending over the entire range of t for $U_x \simeq 1$. This is naturally explained by figure 8 where, for a narrow range of U_x , many ionization levels have similar abundances. Line locking is, in general, less important for less shielding where the UV flux is unattenuated.

The contribution of N V $\lambda 1240$ locking to the total radiation pressure force is of great importance in the study of BAL flows. CN03 have shown that the contribution of N V $\lambda 1240$ is $\sim 1\%$ for non-shielded, solar metallicity gas. We have recalculated this contribution for shielded flows and show the results in figure 10. The contribution of N V $\lambda 1240$ to M remains small as long as the UV bump contributes considerably to the total flux. Larger shield-

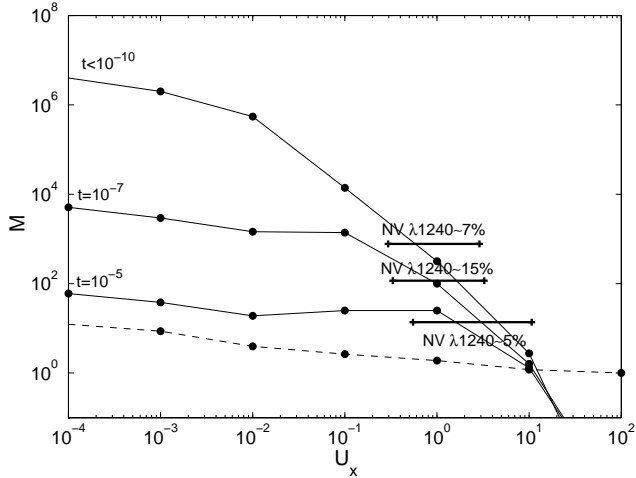


Figure 10. M_{bb} (solid line) and M_{bf} (dashed line) for various values of t for model 3 shielding. Note the rapid decline of M_{bb} with t . The range of U_x where N V $\lambda 1240$ contributes significantly to M is marked next to each curve. As shown, N V $\lambda 1240$ contribution is significant for ionized shielded flows.

Line	τ_l	M_l
model 2 $U_x = 1$ ($M_{bb} = 5$)		
Ne v $\lambda 359$	2.2	0.15
C iv $\lambda 245$	1.5	0.14
N iv $\lambda 247$	2.3	0.13
H i $\lambda 1217$	0.18	0.11
Si x $\lambda 276$	1.1	0.11
C iv $\lambda 1549$	44	0.04
model 3 $U_x = 8$ ($M_{bb} = 3.3$)		
H i $\lambda 1217$	1.3	0.6
H i $\lambda 1027$	0.2	0.2
N iii $\lambda 991$	0.5	0.16
N v $\lambda 1238$	5	0.13
C iii $\lambda 978$	20	0.1
C iv $\lambda 1549$	16	0.07

Table 2. Contribution of the most important lines to the force multiplier assuming $t = 10^{-4}$. Note that for model 3 shielding, only near UV and optical lines participate in driving the gas since the continuum is devoid of far UV photons. The gas temperature in both cases is 4×10^4 K.

ing extinguishes the UV flux above the H I edge and increases the relative contribution of this line. The total contribution to M , for model 3 shielding, is $\sim 10\%$ for a wide range of t and U_x . Thus, for model 3 shielding and typical L_α emission line, the radiation pressure force due to N V $\lambda 1240$ is larger than 50% of the total force (note that in figure 10, the contribution of N V $\lambda 1240$ was calculated relative to the continuum level). For model 4 shielding, the relative contribution of N V $\lambda 1240$ declines due to the lower fractional abundance of N V as a result of the more uniformly distributed ionization structure.

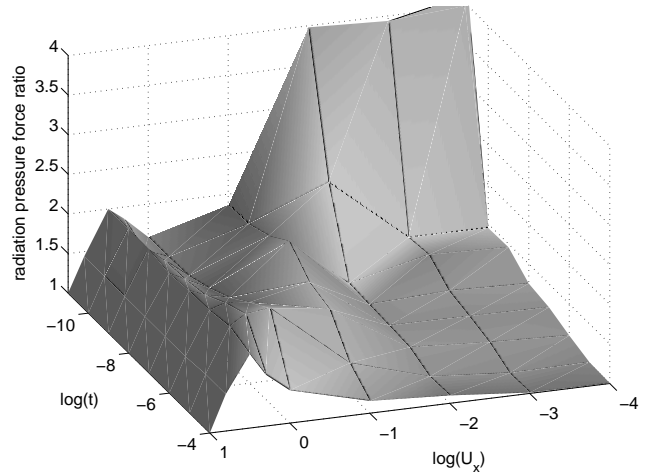


Figure 11. The effect of line locking on the radiation pressure force for model 3 shielded gas. The ratio of radiation pressure force when line locking is accounted for to the case where it is neglected is shown as a function of U_x and t . Emission line properties were taken from Teffler et al. (2002). The effect of L_α locking becomes important for optically thin, low ionization flows and diminishes rapidly with t as L_α becomes optically thick and with U_x due to decreased abundance of H I. The contribution of C IV $\lambda 1549$, N V $\lambda 1240$, O VI $\lambda 1035$ is significant along the ridge at $U_x \gtrsim 1$ (see text).

5 THE DYNAMICS OF SHIELDED FLOWS

We calculated several self-consistent dynamical flow models in order to answer some of the key questions raised in section 1. These include the effect of shielding on the flow dynamics and a qualitative comparison of our model predictions to UV and X-ray observations of BALQSOs. The calculations make use of the non-Sobolev formalism described in CN03. In all subsequent calculations we assume $L_{tot} = 10^{45}$ erg s $^{-1}$ intrinsic type-I AGN continuum, and neglect gravity relative to F_{rad} .

5.1 The effect of shielding on the flow velocity

We first study the effect of shielding on the dynamics of a flow launched from $r_0 = 10^{18}$ cm and characterized by $U_x(r_0) = 10^{-2}$. The velocity profile of shielded and unshielded flows with such properties are shown in figure 12. The most important conclusion is that shielded flows can be accelerated to much larger velocities. Moderate shielding (model 2) suppresses the ionization level and maintains a large radiation pressure force due to the intense continuum below the He II edge. This drives the flow to higher velocities compared to more ionized unshielded flows (factor 4 difference in the terminal velocity). Model 3 shielding results in a lower ionization flow which is driven mainly by H I and He II lines. Such lines become optically thick already at small t . This and the large deficit in UV driving photons result in a lower velocity flow (factor ~ 2 lower than model 2 shielding). Even heavier shielding results in an almost neutral flow whose lines are optically thick and cannot effectively drive the flow to high velocities.

Next we check whether our dynamical model can explain the properties of BALQSOs. Such flows are characterized by UV and X-ray column densities of $\sim 10^{22}$ cm $^{-2}$ (Arav, Korista, & de Kool 2002, Gallagher et al. 1999, 2001, 2002) and typical BAL velocities of order 10,000 km s $^{-1}$. This is done in the context of spherically expanding continuous flows (equation 2) where $U_x \propto v$. Consider

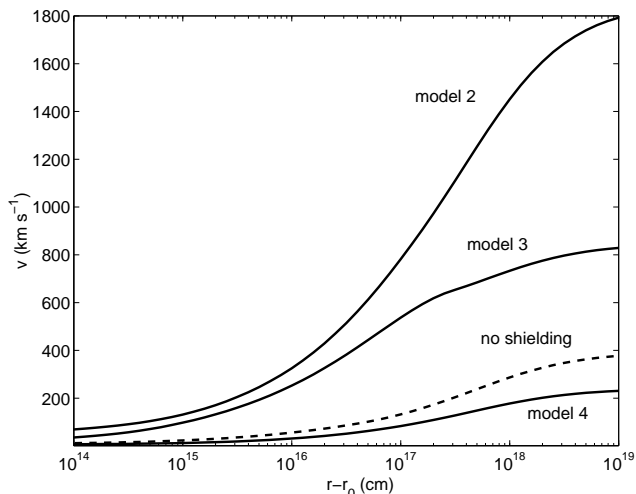


Figure 12. The effect of different types of shield on the dynamics of a flow with given initial conditions (see text). Moderate shielding tends to increase the terminal velocity of the flow. Heavy shielding lowers the terminal velocity.

model 2 shielding and note that in order for the flow to show UV absorption features, its ionization parameter must be smaller than 10 (otherwise it would be fully ionized, see figure 4). Thus, if the BAL trough extends to $\sim 10^4$ km s $^{-1}$ then the entire observed part of the flow must have $U_x < 10$. Given the $U_x \propto v$ dependence, the part of the flow that is traveling with ~ 1000 km s $^{-1}$ would have $U_x < 1$.

We have looked for a model which satisfies those conditions and reproduces the typical velocities and column densities of BAL flows. We assumed an initial velocity of 1000 km s $^{-1}$ and $U_x(r_0) = 1$ (the overall properties are insensitive to these numbers) and calculated velocity profiles for several launching radii r_0 . The results are shown in figure 13). The column density of the flow is obtained by integrating over the density profile. Our calculations show that in order to reach high velocities, the flow has to be launched close to the central source ($r_0 < 10^{17}$ cm) which results in a large column density ($\gg 10^{22}$ cm $^{-2}$). Heavier shielding and smaller $U_x(r_0)$ yield similar results.

The above spherically symmetric continuous flow models cannot account for the observed dynamics and spectral features of BAL flows since they result in column densities larger than observed. One possible solution suggested by Arav & Li (1994) is that such flows consist of small clouds that occupy only a small fraction, ϵ , of the entire volume. These authors assume a continuity equation of the form

$$\epsilon \rho r^2 v = \text{const}, \quad \rho \propto r^{-2}. \quad (6)$$

Self-consistent velocity solutions for such flows that are launched from $\leq 10^{18}$ cm with $\epsilon(r_0) = 0.3$ are shown in figure 13 (dashed lines). Such models are consistent with observations in terms of their column density and terminal velocity. While alternative solutions to the apparent discrepancy between models and observations will not be considered here, we note that it is entirely possible that different parts of the flow suffer different shielding. The full treatment of such multi-phase flows is beyond the scope of this paper.

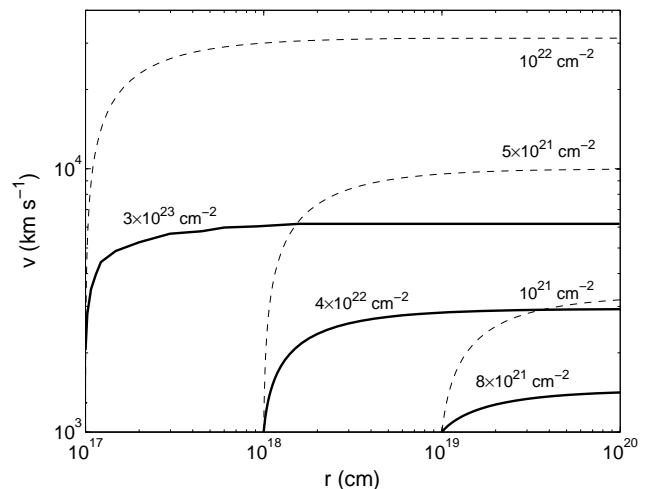


Figure 13. The velocity profile and column densities of model 2 shielded flows for various launching radii. High velocity flows require large column densities and are inconsistent with observations. Flows which occupy only a small fraction of the volume ($\epsilon(r_0) = 0.3$) have smaller column densities and higher velocities compared to continuous flows (dashed lines).

5.2 Line locking

Next we study the effect of line-locking on the flow dynamics and spectral features for the geometry specified by equation 6 and for a small filling factor $\epsilon(r)$.

Figure 14 compares the velocity profiles of model 3 shielded flows which are exposed to a) pure continuum and b) continuum and emission lines. The initial parameters are: $U_x = 0.5$, $r_0 = 3 \times 10^{16}$ cm, $\epsilon(r_0) = 0.03$, $v_0 = 30$ km s $^{-1}$. The first and most important result is that the terminal velocity when emission lines are included is a few times higher than the terminal velocity when the flow is exposed only to the AGN continuum. The effect is more pronounced for low velocity, optically thin flows (see CN03).

The dynamical effect of the N V $\lambda 1240 - L_\alpha$ locking is very important. The velocity profile for a flow which is affected by line locking is shown in figure 14 where it is compared to a canonical wind velocity profile $v = v_\infty(1 - r_0/r)^{1/2}$ (e.g., Castor, Abbott, & Klein 1975; hereafter CAK) with the same terminal velocity but without line locking (dashed line; this model requires different initial conditions). The resulting velocity profile is considerably different: At low velocities ($\lesssim 1000$ km s $^{-1}$), self line locking dominates and the acceleration is larger than the CAK solution. At intermediate velocities ($1000 \lesssim v \lesssim 4000$ km s $^{-1}$) the exact calculation accelerates more slowly than the CAK model since the latter must be more optically thin in order to reach the same terminal velocity. At larger velocities ($\gtrsim 4000$ km s $^{-1}$), N V $\lambda 1240 - L_\alpha$ locking becomes important and the flow accelerates faster than the CAK solution. The absorption line profile of C IV $\lambda 1549$ which results from this velocity profile is shown in figure 15a. This line profile traces the distribution of the radiation pressure force (figure 15b). At low velocities its optical depth per unit velocity, $\tau_v(\text{C IV } \lambda 1549)$, is small due to the rapid acceleration by self-line locking. As the acceleration decreases, $\tau_v(\text{C IV } \lambda 1549)$ increases. For $v \gtrsim 3000$ km s $^{-1}$, the N V $\lambda 1240$ line is exposed to the enhanced flux level of the L_α emission line, the radiation pressure force rises, and the C IV $\lambda 1549$ optical depth decreases (roughly tracing the L_α emission profile). Once $v \gtrsim 6000$ km s $^{-1}$, N V $\lambda 1240 - L_\alpha$ blanketing becomes important, M declines and the line profile saturates.

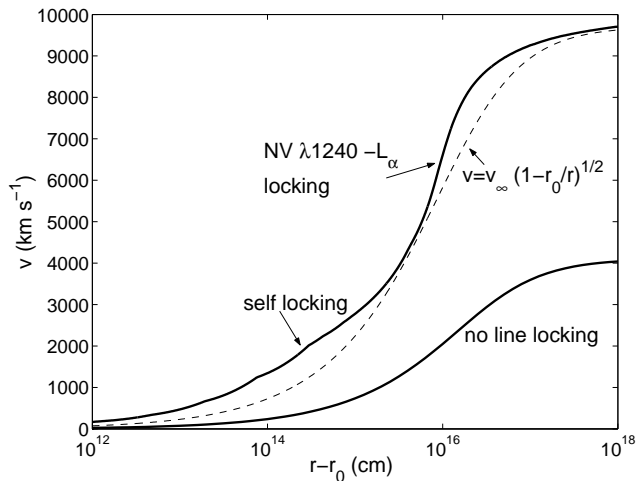


Figure 14. The velocity profile of a flow exposed to continuum and broad emission lines. A canonical wind solution with the same terminal velocity is shown for comparison (dashed line). Note the large deviations from the canonical model due to self line locking and $N\text{ v } \lambda 1240 - L_\alpha$ locking. The terminal velocity of the pure continuum accelerated is a factor ~ 2 lower compared to the full calculation.

The calculated line profile is not unique to CIV $\lambda 1549$ and appears also in other lines. Such line profiles have been observed in several BALQSOs and were termed “the ghost of L_α ” (Arav 1996). Our calculations show that this feature is very sensitive to the abundance of nitrogen and to the UV flux above the H I edge. In particular, the feature is not created for optically thin H I edges. (see also Arav 1996).

6 CONCLUSIONS AND SUMMARY

We have presented detailed photoionization and dynamical calculations for shielded flows in AGN. This allows us to answer some of the questions raised in section 1:

(i) The peculiar shape of the shielded ionizing continuum introduces profound changes in the ionization structure of all flows. Most notable are the lowering of the level of ionization and the almost uniform ionization structure of most metals in highly ionized flows. This may elevate the need for multi-zone models to explain the wide range of ionization levels observed in BAL flows (Turnshek et al. 1996).

(ii) The flow dynamics is determined by its level of ionization and the shape of the ionizing continuum. It is therefore highly sensitive to the properties of the shield and to the UV flux above the Lyman edge. Moderate shielding is most effective in driving the gas to high velocities. Heavy shielding, which absorbs a large fraction of the UV and X-ray flux, results in lower velocities compared to unshielded flows. The calculations show that self line locking and $N\text{ v } \lambda 1240 - L_\alpha$ line locking can have a substantial effect on the flow dynamics and spectral appearance. Internal radiation pressure can considerably affect the dynamics of optically thick, subsonic flows.

(iii) Spherically expanding flows cannot account, self-consistently, for the typically observed velocities and column densities of BAL flows. One possible explanation explored here is a small filling factor flow that occupies only a small fraction of the

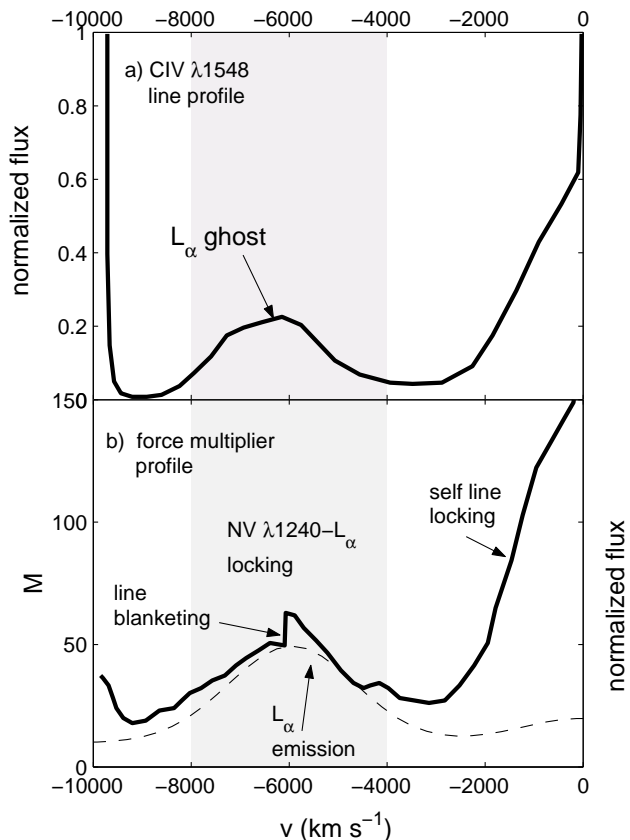


Figure 15. The formation of the “ghost of L_α ” feature. (a) the CIV $\lambda 1549$ line profile showing the double trough feature (Arav 1996) (b) The radiation pressure force as a function of the flow velocity with the effects of self line locking and $N\text{ v } \lambda 1240 - L_\alpha$ locking. Note that the radiation pressure force traces the L_α emission line profile (shown in arbitrary units as dashed line) and the CIV $\lambda 1549$ trough. The sharp drop in M at $v = -6000\text{ km s}^{-1}$ is due to $N\text{ v } \lambda 1240 - L_\alpha$ blanketing. The shaded area highlights the velocity range where $N\text{ v } \lambda 1240 - L_\alpha$ locking is dynamically important.

volume. This helps to explain the formation of BAL troughs that extend over several decades in velocity.

(iv) Our calculations show that it is possible to explain observed BAL features using detailed non-Sobolev modelling. Specifically, we were able to account for the shape of the “ L_α ghost” observed in some BALQSOs. This opens a new avenue for the determination of flow properties such as the location, geometry, ionization structure, and mass flow rate.

We acknowledge financial support by the Israel Science Foundation grant no. 545/00, and the Jack Adler Chair of Extragalactic Astronomy.

REFERENCES

- Arav N., Li Z., Begelman M. C., 1994, *ApJ*, 432, 62
 Arav N., 1996, *ApJ*, 465, 617
 Arav N., Korista K. T., de Kool M., Junkkarinen V. T., Begelman M. C., 1999, *ApJ*, 516, 27
 Arav N., Becker R. H., Laurent-Muehleisen S. A., Gregg M. D., White R. L., Brotherton M. S., de Kool M., 1999, *ApJ*, 524, 566
 Arav N., Korista K. T., de Kool M., 2002, *ApJ*, 566, 699
 Brandt W. N., Laor A., Wills B. J. 2000, *ApJ*, 528, 637
 Bottorff M. C., Korista K., Shlosman I., 2000, *ApJ*, 537, 134

- Castor J., Abbott D., Klein R., 1975, *ApJ*, 195, 157
Chelouche D., Netzer H., 2001 *MNRAS*, 326, 916
Chelouche D., Netzer H., 2003 *MNRAS*, in press
Crenshaw D. M., Kraemer S. B., Bogess A., Maran S. P., Mushotzky R. F., Wu C., 1999, *ApJ*, 516, 750
de Kool M., Arav N., Becker R. H., Gregg M. D., White R. L., Laurent-Muehleisen S. A., Price T., Korista K. T., 2001, *ApJ*, 548, 609
Elitzur M., Ferland G., 1986, *ApJ*, 305, 35
Everett J. E., Konigl A., Arav N., 2002, *ApJ*, 569, 671
Gallagher S. C., Brandt W. N., Sambruna R. M., Mathur S., Yamasaki N. 1999, *ApJ*, 519, 549
Gallagher S. C., Brandt W. N., Laor A., Elvis M., Mathur S., Wills B. J., Iyomoto N. 2001, *ApJ*, 546, 795
Gallagher S. C., Brandt W. N., Chartas G., Sambruna R., 2002, *ApJ*, 567, 37
George I. M., Turner T. J., Netzer H., Nandra K., Mushotzky R., Yaqoob, T., 1998, *ApJS*, 114, 73
Green P. J., Aldcroft T. L., Mathur S., Wilkes B. J., Elvis M. 2001, *ApJ*, 558, 109
Korista K., Hamann F., Ferguson J., Ferland G., 1996, *ApJ*, 461, 641
Koenigl A., Kartje J. F., 1994, *ApJ*, 434, 446
Krolik J. H., 1979, *ApJ*, 228, 13
Krolik J. H. Kriss G. A. 2001, *ApJ*, 561, 684
Mathews W. G., Blumenthal G. R., 1977, *ApJ*, 214, 10
Mathur S., Wilkes B., Elvis M., Fiore F., 1994, *ApJ*, 434, 493
Murray N., Chiang J., Grossman S. A., Voit G. M., 1995, *ApJ*, 451, 498
Netzer H., 1996, *ApJ*, 473, 781
Proga D., Stone J. M., Kallman T. R., 2000, *ApJ*, 543, 686
Stevens I. R., 1991, *ApJ*, 379, 310
Telfer R. C., Zheng W., Kriss G. A., Davidsen A. F., 2002, *ApJ*, 565, 773
Turnshek D. A., Kopko M., Moneir E., Noll D., Espey B. R., Weymann R. J., 1996, *ApJ*, 463, 110